PHYSICAL REVIEW APPLIED **21,** 054047 (2024)

Heralded initialization of charge state and optical-transition frequency of diamond tin-vacancy centers

Julia M. Brevoord,[*,‡] Lorenzo De Santis,[‡] Takashi Yamamoto, Matteo Pasini, Nina Codreanu,
Tim Turan, Hans K.C. Beukers, Christopher Waas, and Ronald Hanson[†]
QuTech and Kavli Institute of Nanoscience, Delft University of Technology, 2628 CJ Delft, Netherlands

(Received 23 November 2023; revised 5 April 2024; accepted 24 April 2024; published 23 May 2024)

Diamond tin-vacancy centers have emerged as a promising platform for quantum information science and technology. A key challenge for their use in more-complex quantum experiments and scalable applications is the ability to prepare the center in the desired charge state with the optical transition at a predefined frequency. Here we report on heralding such successful preparation using a combination of laser excitation, photon detection, and real-time logic. We first show that fluorescence photon counts collected during an optimized resonant probe pulse strongly correlate with the subsequent charge state and optical-transition frequency, enabling real-time heralding of the desired state through threshold photon counting. We then implement and apply this heralding technique to photoluminescence-excitation measurements, coherent optical driving, and an optical Ramsey experiment, finding strongly increased optical coherence with increasing threshold. Finally, we demonstrate that the prepared optical frequency follows the probe laser across the inhomogeneous linewidth, enabling tuning of the transition frequency over multiple homogeneous linewidths.

DOI: 10.1103/PhysRevApplied.21.054047

I. INTRODUCTION

In the past decade, color centers in diamond have become a leading platform for quantum networking experiments [1–3]. The first demonstrations relied on the nitrogen-vacancy center, ranging from the first loophole-free Bell test [4] to multinode-network experiments [5,6]. However, the nitrogen-vacancy center suffers from a low Debye-Waller factor and strong spectral diffusion close to surfaces, making its optical interface inefficient. Group-IV vacancy centers emerged as a favorable alternative due to their high Debye-Waller factor [2,7,8] and inversion symmetry [9], resulting in first-order insensitivity to charge noise [10] and thus compatibility with nanophotonics integration [11,12]. Pioneering experiments showing basic network-node operation in a dilution refrigerator have been performed with the silicon-vacancy center in nanophotonic devices [13–15]. More recently, the negatively charged tin-vacancy [$(\text{Sn-}V)^-$] center in diamond has attracted significant interest because of a high quantum efficiency [7,11,16] and significant spin-orbit coupling, which allows operation at elevated temperatures compared with the silicon-vacancy center [7,17,18]. In recent experiments, the integration of Sn-V centers into nanophotonic devices [19–22] and coherent Sn-V spin-qubit control have been demonstrated [23,24].

It has been widely reported that under resonant optical excitation the $(\text{Sn-}V)^-$ center can go into a dark state [7,17,18,20,25], possibly the $(\text{Sn-}V)^{2-}$ state [26]. Off-resonant excitation (typically around 515–532 nm) is routinely used for repumping to the $(\text{Sn-}V)^-$ state [10,17,19,20]. The optical-transition frequency of the $(\text{Sn-}V)^-$ center after the repump is, in general, not the same as before (spectral diffusion), possibly caused by the capture or release of nearby charges in the repump process or by the direct impact of the pump excitation on the charge environment [26]. The sensitivity of the $(\text{Sn-}V)^-$ center to its charge environment persists in higher orders, despite being first-order insensitive due to inversion symmetry [10]. These processes pose two challenges for future use in quantum protocols: (i) the charge-state repump is probabilistic, leading to initialization errors, and (ii) spectral diffusion hinders efficient optical spin initialization and readout and causes reduced photon indistinguishability, which negatively impacts key protocols requiring photon interference such as remote entanglement generation [27]. In this work, we overcome these challenges by realizing heralded initialization into the desired charge state and preset the optical-transition frequency.

---

[*] Corresponding author: j.m.brevoord@tudelft.nl
[†] Corresponding author: r.hanson@tudelft.nl
[‡] These authors contributed equally to this work.

II. EXPERIMENTAL SETUP

A simplified level structure of the Sn-*V* center in the negatively charged state [(Sn-*V*)$^-$] is shown in Fig. 1(a). In the absence of a magnetic field, the ground and optically excited states consist of spin-degenerate orbital doublets, leading to four optical transitions. Of main interest for a spin-photon interface is the zero-phonon-line (ZPL) transition at 619 nm, linking the lowest-branch ground and optically excited states. Besides the ZPL path, photon emission can be accompanied by the excitation of vibronic modes [phonon-sideband PSB) emission].

Our main investigation focuses on a (Sn-*V*)$^-$ center [labeled "(Sn-*V*)$^-$A"] in an IIa ⟨111⟩-oriented diamond, where Sn ions are implanted approximately 1 nm below the surface. Subsequently, overgrowth of the diamond by chemical-vapor deposition [28] results in (Sn-*V*)$^-$ centers approximately 550 nm below the surface. All experiments on (Sn-*V*)$^-$A are performed in an optical confocal setup at 4 K (see Supplemental Material [29] for experimental setup details). Figure 1(b) shows the second-order correlation function $g^{(2)}$ of the PSB emission of the (Sn-*V*)$^-$ center under continuous resonant excitation. We find $g^{(2)}(0) = 0.10 \pm 0.02$ without any background subtraction, showing that the light indeed originates from an individual emitter.

III. DYNAMICS OF CHARGE STATE AND RESONANCE FREQUENCY

We investigate the (Sn-*V*)$^-$ center by performing photoluminescence-excitation (PLE) scans, where the optical transition is scanned with a resonant laser of 3 nW at approximately 1.3 GHz/s while the PSB emission is recorded. In this experiment, a conditional repump is used: we apply a repump pulse if the peak photon count detected during the PLE is below a preset threshold; see the pulse sequence in Fig. 1(c).

Figure 1(d) shows 1000 consecutive resonant scans. We identify three different regimes, which we label by color on the right for a subset of scans. Red indicates that the optical transition is found near zero detuning ("on resonance") and the photon-count threshold is met. This condition constitutes the desired state. Green indicates scans with counts below the threshold, indicating the emitter has gone into the dark state. A 515-nm repump pulse of 50 ms and 1 μW is applied before the following scan. It can be seen that the repump pulse indeed brings the emitter back to the bright (Sn-*V*)$^-$ state with good probability, often accompanied by a shift of the resonant frequency of the emitter. We highlight scans in orange in which the threshold of counts is met but the detected resonance is significantly detuned, more than 100 MHz ("off resonance"). Importantly, we find that the (Sn-*V*)$^-$ center exhibits high spectral stability both for the on-resonance condition and for the off-resonance condition, up to the point that ionization occurs.

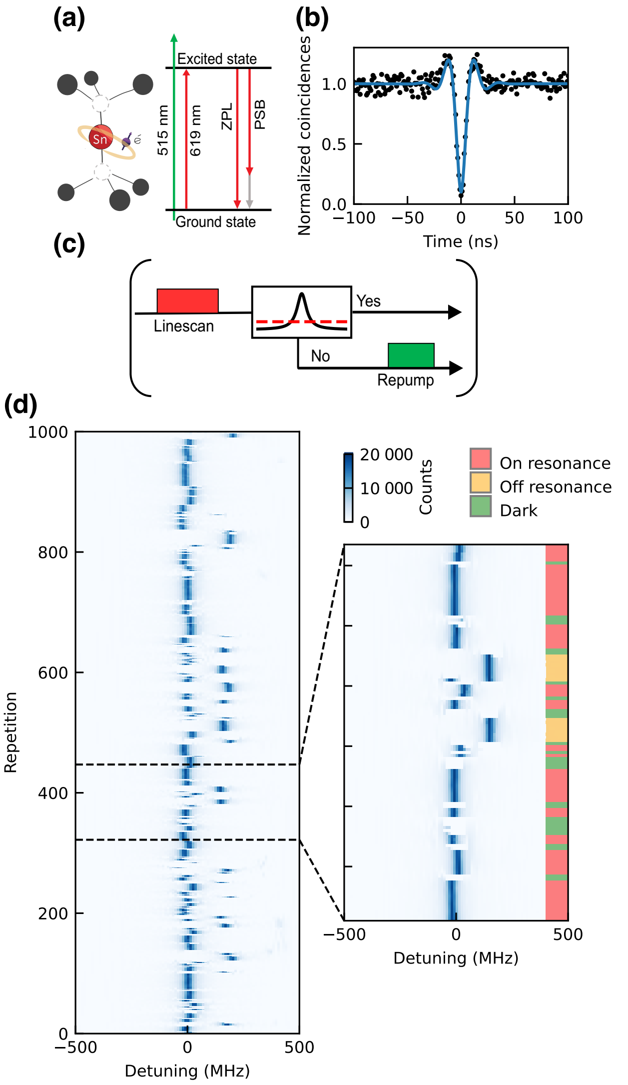

FIG. 1. (a) Color-center structure and the optical transition of interest of a (Sn-*V*)$^-$ center in diamond. Resonant excitation at 619 nm results in emission in the ZPL or PSB decay channels. (b) Second-order correlation measurement of the emission from a single (Sn-*V*)$^-$ center under continuous resonant excitation of 80 nW, fitted by $g^{(2)}(\tau) = 1 - e^{(-3\tau\gamma/4)}(\cos(\omega\tau) + (3\gamma/4\omega)\sin(\omega\tau))$, yielding $g^{(2)}(0) = 0.10 \pm 0.02$, without background correction. (c) Pulse sequence for the conditional PLE measurements, where we apply a repump pulse if the maximum number of photon counts detected during a single frequency step is less than 1.5 times the mean number of photons detected. (d) Fluorescence from 1000 PLE scans taken at approximately 1.3 GHz/s over the optical transition. The state of the emitter is estimated from the counts detected during each scan. If the emitter is flagged as dark, an off-resonant 515-nm pulse is applied before the following scan.

IV. PROBE PULSES FOR CHARGE-STATE AND RESONANCE-CONDITION DETECTION

Motivated by the observed spectral stability before ionization, we explore the possibility of using photon counts during a resonant probe pulse as a heralding signal for the successful preparation of the Sn-V center in the negative charge state with its optical transition at a desired frequency. To gain quantitative insights into the predictive capabilities of such a heralding signal, we implement the pulse sequence shown in Fig. 2(a). A 515-nm "repump" pulse is followed by two identical resonant-laser pulses, named here "pulse 1" and "pulse 2." The sequence in Fig. 2(a) was executed 10 000 times in our experimental runs.

In Fig. 2(b) we plot on a logarithmic scale the distributions of the photons detected during pulse 2, C_2, as a function of the number of photons detected during the preceding pulse 1, C_1, for three different resonant-laser powers. We quantitatively describe the relation between the two distributions C_1 and C_2 via the correlation coefficient $R_{1,2}$ (see Supplemental Material [29] for details). For the lowest power (top panel), we find an almost-perfect correlation of $R_{1,2} = 0.961$. This observation implies that the number of photons scattered by the $(\text{Sn-}V)^-$ center during these pulses is dictated by their charge state and their instantaneous detuning from the laser frequency. By increasing the resonant-laser power (middle and lower panel), we observe a change in the distribution of photon counts. As expected, the mean number of photon counts is increased. In addition, while the correlation between C_1 and C_2 is still present, we can see the effect of ionization, resulting in vertical and horizontal regions of uncorrelated photon distributions with decreasing correlations coefficients $R_{1,2}$ of 0.857 and 0.798, respectively. The vertical band is due to ionization during pulse 2 after several photons have already been detected. The horizontal band corresponds mainly to cases where ionization occurred during pulse 1; those cases could lead to an incorrect heralding signal and should thus be minimized.

Having confirmed that the probe signal strongly correlates to the state of the $(\text{Sn-}V)^-$ center after the probe, we now use this to condition our dataset to cases where the $(\text{Sn-}V)^-$ center is on resonance with the probe laser (i.e., a high number of photon counts in the detection window). As shown in Fig. 2(c), if conditioning is done on $C_1 > 100$, the photon-count distribution of pulse 2 follows a Poisson distribution centered at 110 counts, while the reverse conditioning shows a broader, lower-count distribution mixed with a peak near zero counts. The thresholding approach demonstrated here allows us to filter the desired bright-state condition of the color center out of the statistical distribution of possible charge-resonance states. We determine a lower bound for the initialization fidelity of $(96 \pm 4)\%$ (see Supplemental Material [29] for details). Tighter thresholding can be done at the expense of a decrease in efficiency, as shown in Fig. 2(d). For instance, for the threshold value of 100 used above, we observe a success probability of passing the threshold of 33%.

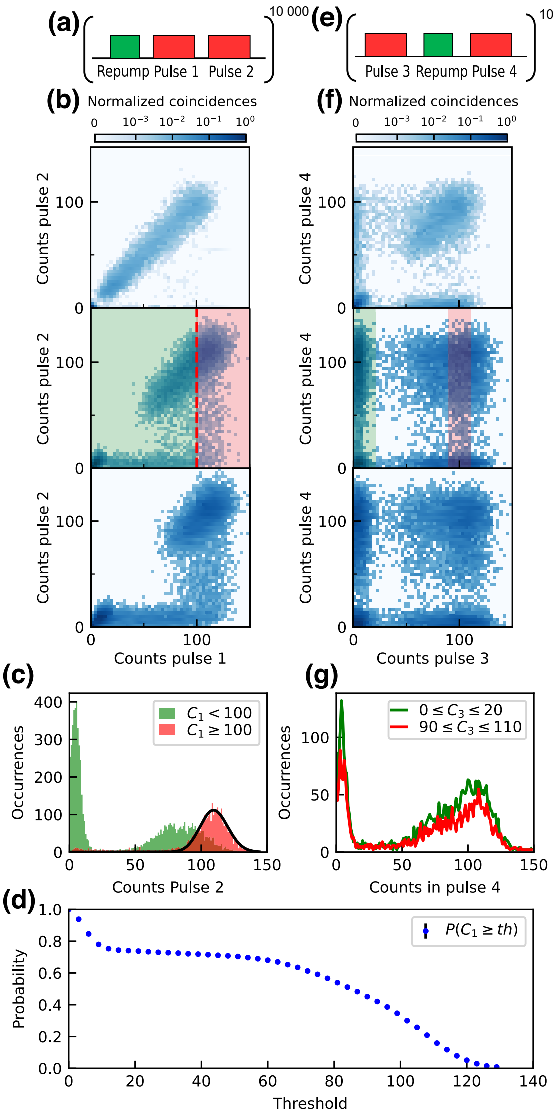

FIG. 2. (a) Pulse sequence used for the data in (b), consisting of an off-resonant pump pulse followed by two identical resonant probe pulses (1 and 2). (b) Two-dimensional histogram of photon counts C_2 as a function of C_1 for increasing resonant-laser powers (10, 100, and 200 nW) and a fixed duration of 50 μs. (c) Histogram of C_2 conditioned on C_1 above or below a threshold of 100 counts of the data from the middle panel in (b). From the former, we determine a lower-bound initialization fidelity of $(96 \pm 4)\%$. The total variance distance of the two histograms is 0.68, which indicates a high degree of orthogonality between the two distributions. (d) Probability of passing the threshold used for heralded bright-state initialization; the error bars fall within the data points. (e) Pulse sequence used for the data in (f), consisting of two identical resonant probe pulses (3 and 4) with an off-resonant pump pulse in between. (f) Two-dimensional histogram of photon counts C_4 as a function of C_3 for increasing repump duration and power (50 μs at 10 μW, 500 μs at 100 μW, and 750 μs at 200 μW). (g) Histogram of C_4 conditioned on C_3 being a low or high number of counts. The total variance distance of the two histograms is 0.09, which indicates a low degree of orthogonality between the two distributions.

Similarly to the analysis above, we study the effect of the repump laser [see pulse sequence in Fig. 2(e)] by plotting the number of photons detected during pulse 4, C_4, as a function of the number of photons detected in the probe pulse (C_3) preceding a pump pulse; see Fig. 2(f). For weak repump pulses (top panel), some correlation between the probe and pump signals is visible, as the repump in this case does not significantly affect the Sn-V center and its environment. For sufficiently strong repump pulses (middle and lower panels), no correlations are observed, showing that the state following the repump pulse is independent of the state before the repump. This is confirmed by the histograms shown in Fig. 2(g), where we plot the count distribution C_4 of the data in the middle panel in Fig. 2(f) for the two shaded areas. We see that the distributions are similar for low and high counts detected in pulse 3.

Using again the data from the middle panel in Fig. 2(f), we estimate how efficiently the repump reinitializes the $(\text{Sn-}V)^-$ center in the negative charge state if it was in the dark state before. For this, we set a threshold of 20 counts to distinguish between the desired charge state and the dark state. Conditioning on a dark state being detected on pulse 3, we find the probability of detecting a bright state on pulse 4 reaches about 75%.

V. OPTICAL RABI DRIVING

Next we investigate the correlation between probe-pulse counts and the $(\text{Sn-}V)^-$ optical coherence. We apply the pulse sequence as shown in Fig. 3(a), where the repump pulse and probe pulse are now followed by 500 repetitions of a 30-ns resonant pulse used to drive optical Rabi oscillations. Figure 3(b) shows a histogram of the number of photons detected during the probe pulse, where three peaks are present. We allocate the instances of high detected photon counts (rightmost peak) to the emitter being in the "on-resonance" state. The instances of the middle and left peak instead correspond respectively to the "off-resonant" and "dark" cases. On the basis of this, we divide the histogram into four parts, as highlighted by the shaded background colors in Fig. 3(b) corresponding to the three peaks described above plus an intermediate region between the center peak and the rightmost peak.

Figure 3(c) shows time traces of the detected photons during the 30-ns resonant readout pulse conditioned on the four threshold intervals. Each curve reveals coherent driven oscillations with different amplitude, frequency, and decay times. As expected, by thresholding for higher probe counts, we obtain higher count rates in the readout, as we are selecting for cases where the $(\text{Sn-}V)^-$ center is on resonance with the driving laser. By fitting these curves with an exponentially damped sine function, we extract the Rabi frequency and decay time of the oscillations. These values are summarized in Fig. 3(d). Since the Rabi frequency is higher for nonzero detuning, this is consistent with the $(\text{Sn-}V)^-$ center being closer to resonance for an increasing number of detected photons in the probe pulse. These results demonstrate a clear relation between the probe counts and the measured coherence.

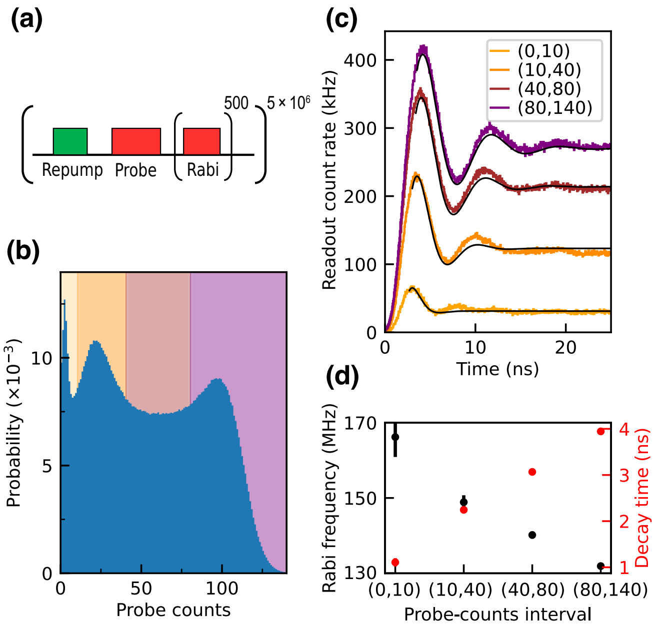

FIG. 3. (a) Pulse sequence used for the Rabi driving experiment conditioned on the probe-pulse counts (repump 500 μs and 100 μW; probe 500 μs and 100 nW; Rabi pulse 30 ns and 17.5 nW). (b) Histogram of the photon counts detected during the probe pulse normalized by the number of sequence iterations. (c) Time-resolved histograms of photon counts during Rabi driving, conditioned on the number of photons detected in the preceding probe pulse. Solid lines are exponentially decaying sine fits to the data. (d) Decay times and Rabi frequencies obtained by our fitting the time traces in (c), including the error of the fits.

VI. REAL-TIME HERALDING OF CHARGE STATE AND OPTICAL-TRANSITION FREQUENCY

In the experiments reported so far, the conditioning on probe-pulse counts was done in postselection. For scalable applications in quantum protocols, it is key that the selection is done in real time, i.e., before quantum protocols are run [5,6,30,31]. In the following, we report implementation of live thresholding on the probe counts using the programmable logic of a fast microcontroller (running on a 10-μs clock cycle, see Supplemental Material [29]) and use this as a charge-resonance-check (CRC) routine to herald the desired charge-resonance state before each experimental run.

The CRC sequence [see Fig. 4(a)] starts with a resonant probe pulse and live counting. Below we report on an implementation using two threshold values instead of

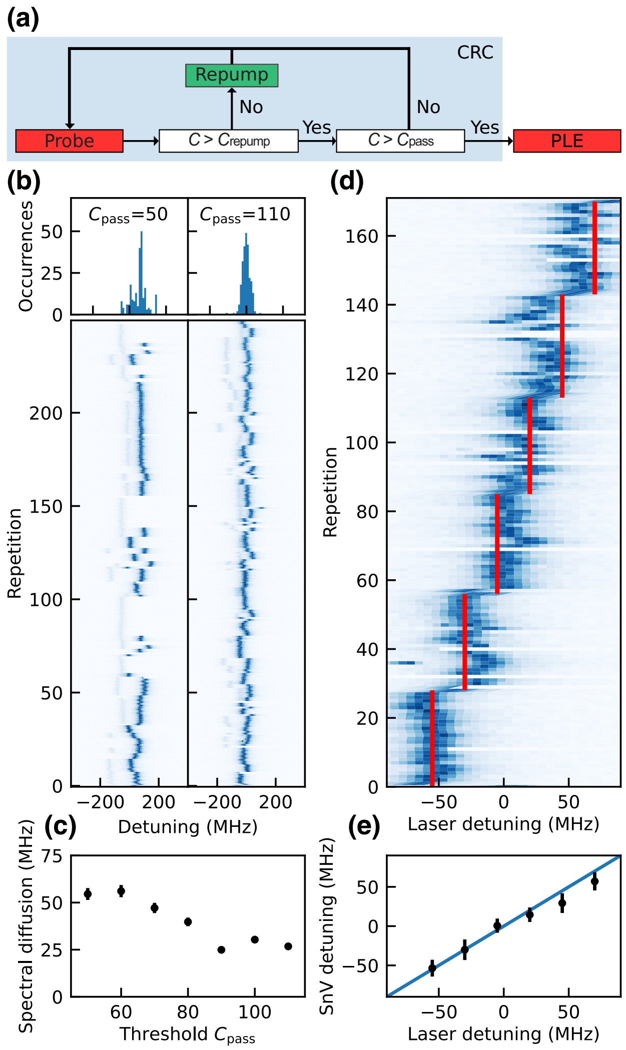

FIG. 4. (a) Real-time logic pulse sequence for the CRC used to herald the charge-resonance state of the Sn-V center. (b) Bottom: Fluorescence from 300 PLE scans each taken at approximately 1.3 GHz/s over the optical transition of $(\text{Sn-}V)^-$A, preceded by a CRC for a threshold C_{pass} of 50 (left) and 110 (right) counts and a threshold $C_{\text{repump}} = 10$. We highlight the presence of a second, weaker resonance in the scans, red detuned with respect to the main one, that we attribute to another nearby emitter. Top: Distribution of the fitted centers of the individual scans, filtered for the bright emitter. (c) Standard deviation of the centers of the individual fitted scans as a function of the CRC threshold. The error bar is the standard error of the standard deviation. (d) Fluorescence from PLE scans each taken at approximately 1.3 GHz/s over the optical transition of $(\text{Sn-}V)^-$B, preceded by a CRC for different resonant frequencies indicated by the vertical red lines. (e) Emitter's mean central frequency as a function of the set laser frequency, showing the shift of the $(\text{Sn-}V)^-$ center's emission by CRC conditioning. The error bar is 1 standard deviation over the repetitions shown in (d).

just one, which allows more freedom in trading off heralding efficiency (rate) and accuracy. If the number of counts detected during the resonant probe pulse is below C_{repump}, an off-resonant 515-nm repump pulse is applied, followed by a resonant probe pulse. If the counts detected during the probe pulse are above C_{repump} but below C_{pass}, the resonant probe pulse is applied again. C_{repump} probes whether the emitter is in the correct charge state and the threshold C_{pass} functions to filter for instances that the emitter is not on resonance with the driving field. This procedure is repeated until the threshold C_{pass} is met.

We first implement the CRC in conjunction with PLE scans to show its effect on spectral diffusion and ionization; see Fig. 4(b). The CRC repump and probe pulses are of the same power and duration as in Fig. 3. Results for 250 PLE scans are shown in Fig. 4(b). Before every scan, a CRC is performed with a threshold (C_{pass}, C_{repump}) of (50, 10) counts for the left panel and (110, 10) counts for the right panel.

For a low CRC threshold, $C_{\text{pass}} = 50$, the $(\text{Sn-}V)^-$ resonant frequency shows spectral jumps less frequently than for a high CRC threshold, $C_{\text{pass}} = 110$, but jumps with higher magnitude. Because of the lower threshold, enough photons can be scattered to pass the CRC even when the $(\text{Sn-}V)^-$ center is off resonance. As a result, these off-resonant cases affect the PLE experiment, while the repump pulse is applied only once the emitter is dark.

With higher CRC thresholding, more repump cycles are required to reach a configuration where the $(\text{Sn-}V)^-$ detuning to the driving laser is small enough to scatter more photons than the threshold value, C_{pass}. This leads to more-frequent spectral jumps of the resonance frequency but the jumps are of significantly lower magnitude. It can be seen how this improves the effective spectral diffusion probed by our experiment by one looking at the distribution of $(\text{Sn-}V)^-$ resonance frequencies in the PLE scans [top panels in Fig. 4(b)]. Here we have filtered for the resonance of the other emitter. In Fig. 4(c), we show the standard deviation of the distribution in the top panel in Fig. 4(b) as a function of the CRC threshold, C_{pass}. A clear trend towards a single-peaked distribution and lower variance is visible for higher thresholds (see Supplemental Material [29] for the PLE scans). We note that use of a CRC threshold $C_{\text{pass}} < 50$ resulted in too few repump pulses to reliably determine the repump-induced spectral diffusion.

In addition, we applied the CRC on a different Sn-V center [$(\text{Sn-}V)^-$B], which is embedded in a nanophotonic waveguide (see Ref. [22] for the device and experimental-setup details). When setting a high C_{pass}, we observe similar stable lines as for $(\text{Sn-}V)^-$A; see Fig. 4(d) and Supplemental Material [29] for more PLE scans obtained with different CRC thresholds. Furthermore, we show on $(\text{Sn-}V)^-$B that the CRC can be used to tune the heralded optical-transition frequency. In Fig. 4(d), we increase the frequency of the resonant laser during the CRC about every 30 scans, while using a high C_{pass}. As a consequence the heralding value of the emitter frequency will also change. The resonant-peak center detected in the subsequent PLE follows the frequency set point indicated by the solid red lines as shown in Fig. 4(d). In Fig. 4(e), we plot the mean center frequency of the individual scans for the different laser-detuning set points. This experiment shows that using CRC heralding, we can tune the emitter by more than 100 MHz, which is several times greater than the measured mean single-scan (homogeneous) linewidth of 31 MHz. The effective tuning range of this method is determined by the inhomogeneous (or spectral-diffusion-limited) linewidth (which can be measured by one setting the CRC threshold to zero), as the probability for the repump pulse bringing the optical transition to more-detuned frequencies decreases rapidly.

VII. OPTICAL RAMSEY EXPERIMENT USING REAL-TIME HERALDING

Finally, we directly probe the coherence of the optical transition for different CRC thresholds by performing Ramsey-interferometry experiments using the pulse sequence depicted in Fig. 5(a). First, coherence between the ground state and the optically excited state is created with an optical $\pi/2$ pulse. After letting this state evolve for time τ, we apply a second $\pi/2$ pulse to map the remaining coherence onto populations that we read out by integrating the fluorescence in a 5-ns window after the second $\pi/2$ pulse. This signal is then normalized to twice the fluorescence measured for a mixed state (i.e., for large τ).

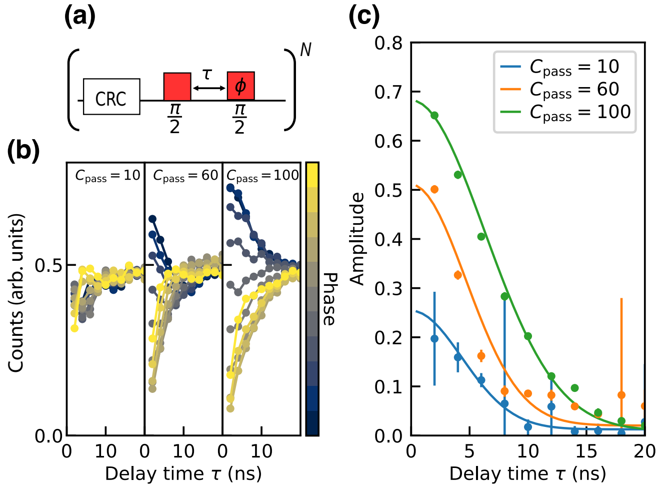

FIG. 5. Optical Ramsey experiment conditioned on CRC. (a) Pulse sequence used for the data in (b),(c) (see Supplemental Material [29] for further details). (b) Counts detected during an integration window after the second $\pi/2$ pulse for fixed C_{repump} of 10 and different values of C_{pass}, for different phases of the second $\pi/2$ pulse, normalized to twice the counts detected in a mixed state. (c) Contrast decay envelopes for different CRC thresholds, C_{pass}, and fixed C_{repump} of 10. The fitted envelopes show an increase of T_2^* from (4.3 ± 1.7) ns for a low threshold, C_{pass}, to (6.3 ± 0.4) ns for the highest C_{pass} of 100. The error bars are fit errors.

We run this experiment for different delays τ and phase differences ϕ of the pulses. The resulting data are shown in Fig. 5(b), where the dependence of the readout signal on τ (x-axis value) and ϕ (plot color) is shown for C_{pass} of 10, 60, and 110 counts in the left, center, and right panels, respectively, and fixed $C_{\text{repump}} = 10$. With increasing CRC threshold C_{pass}, we observe both a higher contrast of the oscillations and a slower decay of this contrast with increasing τ.

We extract a quantitative measure for the coherence between the ground state and the excited state by fitting the phase dependence for each value of τ to a sine function [20]. The amplitude of the sine is plotted in Fig. 5(c) as a function of τ. From a Gaussian fit to the data, we determine the dephasing time T_2^* of the optical transition. For the CRC threshold $C_{\text{pass}} = 10$, we obtain T_2^* of (4.3 ± 1.7) ns, where the large uncertainty is a consequence of the low contrast. For a high CRC threshold $C_{\text{pass}} = 100$, we determine $T_2^* = (6.3 \pm 0.4)$ ns. This is, to our knowledge, the highest measured optical T_2^* for a (Sn-V)$^-$ center to date. This demonstrates that implementation of a CRC can mitigate the effects of spectral detuning, leading to an increase in optical coherence time, which is key to improving photon-interference experiments.

VIII. CONCLUSION AND OUTLOOK

The ability to reliably prepare color-center qubits in the desired charge state at a set optical-transition frequency, as demonstrated here, is a key requirement for efficiently running complex quantum experiments as well for future quantum technologies. Taken together with recent diamond-Sn-V-center demonstrations of nanophotonic integration [19], spin-qubit control, and coherence beyond 1 ms [23,24], our results complete a quantum control toolkit for scaling current single-center experiments. Compared with the experimentally maturer diamond nitrogen-vacancy center [4,5,30,31] and diamond silicon-vacancy center [14,15,32,33], the Sn-V center adds the combination of compatibility with nanophotonic integration and relatively high quantum efficiency and operating temperature, making it a compelling platform for future exploration of multiqubit quantum networking and quantum computing protocols.

The datasets that support this work are available from 4TU.ResearchData [34].

ACKNOWLEDGMENTS

We thank Henri Ervasti for software support. We thank Yanik Herrmann and Julius Fisher for proofreading the manuscript. We gratefully acknowledge support of this work by the Dutch Research Council (NWO) through the Spinoza Prize 2019 (Project No. SPI 63-264), by the

Dutch Ministry of Economic Affairs and Climate Policy (EZK) as part of the Quantum Delta NL program, by the joint research program “Modular quantum computers” of Fujitsu Limited and Delft University of Technology, cofunded by the Netherlands Enterprise Agency under Project No. PPS2007, and by the QIA-Phase 1 project through the European Union’s Horizon Europe research and innovation program under Grant Agreement No. 101102140. L.D.S. acknowledges funding from the European Union’s Horizon 2020 research and innovation program under Marie Skłodowska-Curie Grant Agreement No. 840393.

J.M.B. and L.D.S conducted the experiments and analyzed the data. T.Y. performed the diamond overgrowth. J.M.B. prepared the diamond sample with Sn-V centers, (Sn-V)$^-$A. T.T. helped with the measurements on the waveguide sample, (Sn-V)$^-$B, which was fabricated by N.C., and M.P. designed and built the waveguide setup. C.W., H.K.C.B., J.M.B., L.D.S., and M.P. were involved in building parts of the setup used for the main part of the measurements. J.M.B., L.D.S., and R.H. wrote the manuscript with input from all authors. L.D.S. and R.H. supervised the experiments.

[1] M. Atatüre, D. Englund, N. Vamivakas, S.-Y. Lee, and J. Wrachtrup, Material platforms for spin-based photonic quantum technologies, Nat. Rev. Mater. **3**, 38 (2018).

[2] M. Ruf, N. H. Wan, H. Choi, D. Englund, and R. Hanson, Quantum networks based on color centers in diamond, J. Appl. Phys. **130**, 070901 (2021).

[3] G. Wolfowicz, F. J. Heremans, C. P. Anderson, S. Kanai, H. Seo, A. Gali, G. Galli, and D. D. Awschalom, Quantum guidelines for solid-state spin defects, Nat. Rev. Mater. **6**, 906 (2021).

[4] B. Hensen, H. Bernien, A. E. Dreau, A. Reiserer, N. Kalb, M. S. Blok, J. Ruitenberg, R. F. L. Vermeulen, R. N. Schouten, C. Abellán, W. Amaya, V. Pruneri, M. W. Mitchell, M. Markham, D. J. Twitchen, D. Elkouss, S. Wehner, T. H. Taminiau, and R. Hanson, Loophole-free Bell inequality violation using electron spins separated by 1.3 kilometres, Nature **526**, 682 (2015).

[5] M. Pompili, S. L. N. Hermans, S. Baier, H. K. C. Beukers, P. C. Humphreys, R. N. Schouten, R. F. L. Vermeulen, M. J. Tiggelman, L. Dos Santos Martins, B. Dirkse, S. Wehner, and R. Hanson, Realization of a multinode quantum network of remote solid-state qubits, Science **372**, 259 (2021).

[6] S. L. N. Hermans, M. Pompili, H. K. C. Beukers, S. Baier, J. Borregaard, and R. Hanson, Qubit teleportation between non-neighbouring nodes in a quantum network, Nature **605**, 663 (2022).

[7] T. Iwasaki, Y. Miyamoto, T. Taniguchi, P. Siyushev, M. H. Metsch, F. Jelezko, and M. Hatano, Tin-vacancy quantum emitters in diamond, Phys. Rev. Lett. **119**, 253601 (2017).

[8] C. Bradac, W. Gao, J. Forneris, M. E. Trusheim, and I. Aharonovich, Quantum nanophotonics with group IV defects in diamond, Nat. Commun. **10**, 5625 (2019).

[9] C. Hepp, T. Müller, V. Waselowski, J. N. Becker, B. Pingault, H. Sternschulte, D. Steinmüller-Nethl, A. Gali, J. R. Maze, M. Atatüre, and C. Becher, Electronic structure of the silicon vacancy color center in diamond, Phys. Rev. Lett. **112**, 036405 (2014).

[10] L. De Santis, M. Trusheim, K. Chen, and D. Englund, Investigation of the Stark effect on a centrosymmetric quantum emitter in diamond, Phys. Rev. Lett. **127**, 147402 (2021).

[11] A. Sipahigil, R. E. Evans, D. D. Sukachev, M. J. Burek, J. Borregaard, M. K. Bhaskar, C. T. Nguyen, J. L. Pacheco, H. A. Atikian, C. Meuwly, R. M. Camacho, F. Jelezko, E. Bielejec, H. Park, M. Lončar, and M. D. Lukin, An integrated diamond nanophotonics platform for quantum-optical networks, Science **354**, 847 (2016).

[12] R. E. Evans, M. K. Bhaskar, D. D. Sukachev, C. T. Nguyen, A. Sipahigil, M. J. Burek, B. Machielse, G. H. Zhang, A. S. Zibrov, E. Bielejec, H. Park, M. Lončar, and M. D. Lukin, Photon-mediated interactions between quantum emitters in a diamond nanocavity, Science **362**, 662 (2018).

[13] D. Sukachev, A. Sipahigil, C. Nguyen, M. Bhaskar, R. Evans, F. Jelezko, and M. Lukin, Silicon-vacancy spin qubit in diamond: A quantum memory exceeding 10 ms with single-shot state readout, Phys. Rev. Lett. **119**, 223602 (2017).

[14] M. K. Bhaskar, R. Riedinger, B. Machielse, D. S. Levonian, C. T. Nguyen, E. N. Knall, H. Park, D. Englund, M. Lončar, D. D. Sukachev, and M. D. Lukin, Experimental demonstration of memory-enhanced quantum communication, Nature **580**, 60 (2020).

[15] P.-J. Stas, Y. Q. Huan, B. Machielse, E. N. Knall, A. Suleymanzade, B. Pingault, M. Sutula, S. W. Ding, C. M. Knaut, D. R. Assumpcao, Y.-C. Wei, M. K. Bhaskar, R. Riedinger, D. D. Sukachev, H. Park, M. Lončar, D. S. Levonian, and M. D. Lukin, Robust multi-qubit quantum network node with integrated error detection, Science **378**, 557 (2022).

[16] M. Nguyen, N. Nikolay, C. Bradac, M. Kianinia, E. A. Ekimov, N. Mendelson, O. Benson, and I. Aharonovich, Photodynamics and quantum efficiency of germanium vacancy color centers in diamond, Adv. Photonics **1**, 066002 (2019).

[17] J. Görlitz, D. Herrmann, G. Thiering, P. Fuchs, M. Gandil, T. Iwasaki, T. Taniguchi, M. Kieschnick, J. Meijer, M. Hatano, A. Gali, and C. Becher, Spectroscopic investigations of negatively charged tin-vacancy centres in diamond, New J. Phys. **22**, 013048 (2020).

[18] M. E. Trusheim *et al.*, Transform-limited photons from a coherent tin-vacancy spin in diamond, Phys. Rev. Lett. **124**, 023602 (2020).

[19] A. E. Rugar, S. Aghaeimeibodi, D. Riedel, C. Dory, H. Lu, P. J. McQuade, Z.-X. Shen, N. A. Melosh, and J. Vučković, Quantum photonic interface for tin-vacancy centers in diamond, Phys. Rev. X **11**, 031021 (2021).

[20] J. Arjona Martínez, R. A. Parker, K. C. Chen, C. M. Purser, L. Li, C. P. Michaels, A. M. Stramma, R. Debroux, I. B. Harris, M. Hayhurst Appel, E. C. Nichols, M. E. Trusheim, D. A. Gangloff, D. Englund, and M. Atatüre, Photonic

indistinguishability of the tin-vacancy center in nanostructured diamond, Phys. Rev. Lett. **129**, 173603 (2022).

[21] K. Kuruma, B. Pingault, C. Chia, D. Renaud, P. Hoffmann, S. Iwamoto, C. Ronning, and M. Lončar, Coupling of a single tin-vacancy center to a photonic crystal cavity in diamond, Appl. Phys. Lett. **118**, 230601 (2021).

[22] M. Pasini, N. Codreanu, T. Turan, A. R. Moral, C. F. Primavera, L. De Santis, H. K. C. Beukers, J. M. Brevoord, C. Waas, J. Borregaard, and R. Hanson, Nonlinear quantum photonics with a tin-vacancy center coupled to a one-dimensional diamond waveguide, ArXiv:2311.12927.

[23] E. I. Rosenthal, C. P. Anderson, H. C. Kleidermacher, A. J. Stein, H. Lee, J. Grzesik, G. Scuri, A. E. Rugar, D. Riedel, S. Aghaeimeibodi, G. H. Ahn, K. Van Gasse, and J. Vučković, Microwave spin control of a tin-vacancy qubit in diamond, Phys. Rev. X **13**, 031022 (2023).

[24] X. Guo *et al.*, Microwave-based quantum control and coherence protection of tin-vacancy spin qubits in a strain-tuned diamond-membrane heterostructure, Phys. Rev. X **13**, 041037 (2023).

[25] T. Lühmann, J. Küpper, S. Dietel, R. Staacke, J. Meijer, and S. Pezzagna, Charge-state tuning of single SnV centers in diamond, ACS Photonics **7**, 3376 (2020).

[26] J. Görlitz, D. Herrmann, P. Fuchs, T. Iwasaki, T. Taniguchi, D. Rogalla, D. Hardeman, P.-O. Colard, M. Markham, M. Hatano, and C. Becher, Coherence of a charge stabilised tin-vacancy spin in diamond, npj Quantum Inf. **8**, 45 (2022).

[27] H. K. Beukers, M. Pasini, H. Choi, D. Englund, R. Hanson, and J. Borregaard, Remote-entanglement protocols for stationary qubits with photonic interfaces, PRX Quantum **5**, 010202 (2024).

[28] A. E. Rugar, H. Lu, C. Dory, S. Sun, P. J. McQuade, Z.-X. Shen, N. A. Melosh, and J. Vučković, Generation of tin-vacancy centers in diamond via shallow ion implantation and subsequent diamond overgrowth, Nano Lett. **20**, 1614 (2020).

[29] See Supplemental Material at http://link.aps.org/supplemental/10.1103/PhysRevApplied.21.054047 for a detailed description of the sample fabrication, the experimental-setup details, the optical-π-pulse calibration, and additional data on CRC linescans and CRC Ramsey experiments [35].

[30] S. L. N. Hermans, M. Pompili, L. D. Santos Martins, A. R-P Montblanch, H. K. C. Beukers, S. Baier, J. Borregaard, and R. Hanson, Entangling remote qubits using the single-photon protocol: An in-depth theoretical and experimental study, New J. Phys. **25**, 013011 (2023).

[31] A. Stolk, K. van der Enden, M.-C. Roehsner, A. Teepe, S. Faes, C. Bradley, S. Cadot, J. van Rantwijk, I. te Raa, R. Hagen, A. Verlaan, J. Biemond, A. Khorev, R. Vollmer, M. Markham, A. Edmonds, J. Morits, T. Taminiau, E. van Zwet, and R. Hanson, Telecom-band quantum interference of frequency-converted photons from remote detuned NV centers, PRX Quantum **3**, 020359 (2022).

[32] B. Pingault, D.-D. Jarausch, C. Hepp, L. Klintberg, J. N. Becker, M. Markham, C. Becher, and M. Atatüre, Coherent control of the silicon-vacancy spin in diamond, Nat. Commun. **8**, 15579 (2017).

[33] S. Meesala, Y.-I. Sohn, B. Pingault, L. Shao, H. A. Atikian, J. Holzgrafe, M. Gündoğan, C. Stavrakas, A. Sipahigil, C. Chia, R. Evans, M. J. Burek, M. Zhang, L. Wu, J. L. Pacheco, J. Abraham, E. Bielejec, M. D. Lukin, M. Atatüre, and M. Lončar, Strain engineering of the silicon-vacancy center in diamond, Phys. Rev. B **97**, 205444 (2018).

[34] J. M. Brevoord, L. De Santis, T. Yamamoto, M. Pasini, N. Codreanu, T. Turan, H. K. C. Beukers, C. Waas, and R. Hanson, Data underlying the publication "Heralded initialization of charge state and optical transition frequency of diamond tin-vacancy centers" (Version 1) [Data set], 4TU.ResearchData (2023), https://doi.org/10.4121/39356576-6144-465A-869C-E3E9C35E2DC6.

[35] I. T. Raa, H. K. Ervasti, P. J. Botma, L. C. Visser, R. Budhrani, J. F. van Rantwijk, S. P. A. Cadot, J. Vermeltfoort, M. Pompili, A. J. Stolk, M. J. Weaver, K. L. van der Enden, D. de Leeuw Duarte, M. Teng, J. van Zwieten, and F. Grooteman, QMI – Quantum Measurement Infrastructure, a Python 3 framework for controlling laboratory equipment (2023), https://doi.org/10.4121/6d39c6db-2f50-4a49-ad60-5bb08f40cb52.